



LAWRENCE
LIVERMORE
NATIONAL
LABORATORY

Statistical analysis of non-Maxwellian electron distribution functions measured with angularly resolved Thomson scattering

M. Sherlock, A. L. Milder, J. Katz, R. Boni, J. P. Palastro, W. Rozmus, D. H. Froula

September 14, 2021

Physics of Plasma

Disclaimer

This document was prepared as an account of work sponsored by an agency of the United States government. Neither the United States government nor Lawrence Livermore National Security, LLC, nor any of their employees makes any warranty, expressed or implied, or assumes any legal liability or responsibility for the accuracy, completeness, or usefulness of any information, apparatus, product, or process disclosed, or represents that its use would not infringe privately owned rights. Reference herein to any specific commercial product, process, or service by trade name, trademark, manufacturer, or otherwise does not necessarily constitute or imply its endorsement, recommendation, or favoring by the United States government or Lawrence Livermore National Security, LLC. The views and opinions of authors expressed herein do not necessarily state or reflect those of the United States government or Lawrence Livermore National Security, LLC, and shall not be used for advertising or product endorsement purposes.

Statistical analysis of non-Maxwellian electron distribution functions measured with angularly resolved Thomson scattering

A. L. Milder,^{1,2, a)} J. Katz,¹ R. Boni,¹ J. P. Palastro,¹ M. Sherlock,³ W. Rozmus,⁴ and D. H. Froula^{1,2}

¹⁾*Laboratory for Laser Energetics, 250 E. River Rd, Rochester, NY 14623, USA*

²⁾*Department of Physics and Astronomy, University of Rochester, Rochester, NY 14623, USA*

³⁾*Lawrence Livermore National Laboratory, 7000 East Avenue, Livermore, CA 94550, USA*

⁴⁾*Department of Physics, University of Alberta, Edmonton, Alberta T6G 2E1, Canada*

(Dated: 25 August 2021)

Angularly resolved Thomson scattering is a novel extension of Thomson scattering, enabling the measurement of the electron velocity distribution function over many orders of magnitude. Here, details of the theoretical basis of the technique and the instrument designed for this measurement are described. Angularly resolved Thomson-scattering data from several experiments are shown with descriptions of the corresponding distribution functions. A reduced model describing the distribution function is given and used to perform a Monte Carlo analysis of the uncertainty in the measurements. The electron density and temperature were determined to a precision of 12% and 21%, respectively, on average while all other parameters defining the distribution function were generally determined to better than 20%. It was found that these uncertainties were primarily due to limited signal to noise and instrumental effects. Measurements with this level of precision were sufficient to distinguish between Maxwellian and non-Maxwellian distribution functions.

^{a)}Electronic mail: Corresponding Author: amild@lle.rochester.edu

I. INTRODUCTION

The electron and ion distribution functions dictate the properties and evolution of a plasma. Many of these properties, including energy transport and laser coupling, are primarily determined by the electron velocity distribution function. The electron velocity distribution function is often assumed to be Maxwellian¹⁻⁴ or close to Maxwellian,^{5,6} however the existence of non-Maxwellian electron distribution functions have significant ramifications on the behavior of a plasma.

In 1980, it was predicted that inverse bremsstrahlung heating, the main heating mechanism in laser produced plasmas, preferentially transfers energy to the slower electrons driving a flat-top, or super-Gaussian distribution⁷. The reduction in slow electrons diminishes the inverse bremsstrahlung heating rate and in subsequent years nearly all hydrodynamic models that include laser propagation have introduced a factor to adjust the laser absorption due to this effect^{8,9}. Challenges in measuring the electron distribution function¹⁰⁻¹² have made it difficult to verify these theories, although extensive computational work has been done over the last forty years¹³⁻¹⁸. Computational studies have explored the evolution of the distribution function resulting from inverse bremsstrahlung heating, including the consideration of the relatively small electron-ion collision rate of the fast electrons¹⁹, thermal transport¹⁴, and electron-electron collisions¹⁵, which all tend to produce high-velocity electrons (tails) and a non-Maxwellian bulk of electrons.

In laser-produced plasmas, inverse bremsstrahlung heating is only one of the processes that can alter the electron distribution function. Thermal transport^{20,21}, laser-plasma instabilities²², and atomic kinetic processes²³ all provide competing mechanisms that shape the electron distribution function. Numerous consequences of non-Maxwellian electron distribution functions on laser absorption and laser-plasma instabilities have been predicted^{7,13,14,21,24,25} but are often neglected in models and simulations due to a lack of experimental verification and the computation expense of including a kinetic solver.

Thomson scattering is currently a workhorse diagnostic for temperature and density measurements in many areas of plasma physics²⁶⁻³⁷ and recently it was shown that the electron distribution function could be inferred from collective Thomson scattering, but all previous work required an assumed distribution function either from theory^{25,38} or simulations³⁹. While non-collective Thomson scattering is known to reflect the underlying distribution

function^{40,41}, it suffers from a small scattering cross section, which leads to signal-to-noise limitations. A new technique, angularly resolved Thomson scattering, combines the collective and non-collective regimes in order to directly measure the electron velocity distribution function over many orders of magnitude without an assumption on its underlying shape⁴². The conceptual leap from using Thomson scattering to measure bulk properties or confirm a predetermined distribution function, to a direct measurement of the electron distribution function vastly expands the scope of potential studies. This technique allows Thomson scattering to better discriminate between kinetic theories and distribution functions not yet theorized.

This article examines the precision of the distribution functions measured using angularly resolved Thomson scattering, specifically in context of non-Maxwellian electron distribution functions driven by inverse bremsstrahlung heating. The distribution functions measured in uniform underdense plasmas, created by inverse bremsstrahlung heating of a gas jet plume, were found to be well described by a super-Gaussian + Maxwellian model. The super-Gaussian bulk is associated with inverse bremsstrahlung heating and is well reproduced by previous computational work¹³, while the tail is associated with the isotropy of heating. This new super-Gaussian + Maxwellian model provides a basis for further theoretical investigations of the source of the tail. Markov-chain Monte Carlo analysis was performed using this reduced model to identify a confidence region on the measured electron distribution functions. It was found that electron density and temperature were determined to a precision of 12% and 21%, respectively, on average while all other parameters defining the distribution function were generally determined to better than 20%. These uncertainties were primarily due to limited signal to noise and instrumental effects. Measurements with this level of precision were sufficient to distinguish between Maxwellian and non-Maxwellian distribution functions. Further, the confidence region found for these measurements establish a benchmark for determining when future distribution function measurements will be distinguishable from other hypotheses.

This paper is organized as follows. In Section II the experimental setup and details of the angularly resolved Thomson-scattering instrument are discussed. Section III provides an overview of Thomson scattering and the theoretical basis for angularly resolved Thomson scattering. Section IV discusses the measured distribution function, and a physical basis for interpreting the measurements. Section V describes the methods used to determine the

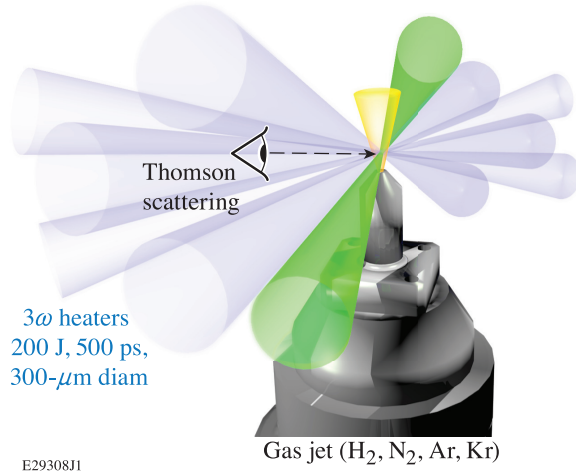


FIG. 1. Schematic of the experimental configuration. Five UV beams (purple) heat the gas (yellow) from a supersonic Mach-3 gas jet (gray). A green beam represents the probe beam used for Thomson scattering.

uncertainties on the measured distribution functions. The paper is summarized in Section VI.

II. EXPERIMENTAL SETUP

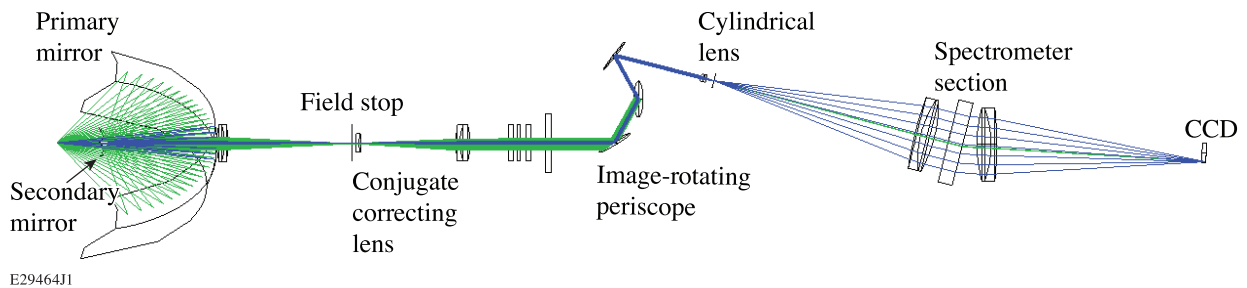


FIG. 2. A wire-frame model of the angularly resolved Thomson-scattering instrument with ray fans, originating in the collection volume, showing the path of sagittal (green) and tangential (blue) rays.

Experiments that measured non-Maxwellian electron distribution functions resulting from laser heating were conducted on the OMEGA Laser System⁴³ at the Laboratory for Laser Energetics. Figure 1 shows the experimental configuration where five ultraviolet (351-nm UV) laser beams were used to ionize and heat a gas. The uniform density neutral gas plume

of argon, krypton, or hydrogen was produced using a supersonic Mach-3 gas jet⁴⁴ with an exit diameter of 2 mm. To improve the uniformity of heating, each of the five UV heating beams used a distributed phase plate, polarization smoothing, and smoothing by spectral dispersion. This ultimately provided Gaussian focal spots, 2 mm above the center of the gas jet, with a $1/e^2$ diameter of 400 μm . The heating beams had a 500-ps pulse duration, full-width at half-maximum (FWHM), and 50 J to 200 J per beam. This resulted in a total overlapped UV intensity of $I_{\text{UV}}^{\text{total}} = 0.62 - 2.8 \times 10^{15} \text{ W/cm}^2$.

A 10-J green (526.5 nm) probe beam was focused to the same location as the heating beams. The probe beam had a shorter 200-ps FWHM duration and was delayed 300 ps or 600 ps from the rise of the heating beams. This allowed Thomson-scattering measurements at the end of the heating or shortly after the heating beams turned off. The probe beam used a distributed phase plate to produce a flattop focal spot with a 100- μm FWHM diameter ($I_{2\omega} = 6.5 \times 10^{14} \text{ W/cm}^2$). Unlike the heating beams, the probe did not employ smoothing by spectral dispersion or polarization smoothing. Instead, the linear polarization was rotated with a waveplate to maximize the Thomson-scattering efficiency and make it uniform as a function of angle.

A. Angularly Resolved Thomson-Scattering Instrument

Figure 2 shows the angularly resolved Thomson-scattering instrument. Light collected from a 50 $\mu\text{m} \times 50 \mu\text{m} \times 100 \mu\text{m}$ Thomson-scattering volume in the plasma was imaged onto a 500 ps time-gated 2-D recording device (Princeton Instruments PI-Max4 gated CCD) with wavelength dispersed along the horizontal axis and scattering angle along the vertical axis. The instrument consists of three optical sections. A custom microscope collects light from the scattering volume and images it onto the field stop that defines the spatial region of interest. An image-rotating relay images the field stop to the input slit of the spectrometer. A spectrometer disperses spectra horizontally at the detector surface, while maintaining emission angle in the vertical direction. The system has an angular resolution of 1° over a 108° range and a 1 nm spectral resolution over a 200 nm spectrum.

The objective of the custom microscope is a modified Schwarzschild design. The primary mirror is a 180 mm \times 50 mm rectangular section cut from the center of an $R = 93.68 \text{ mm}$ concave spherical mirror. This rectangular section of mirror is the 108° (angular scatter-

ing direction) $\times 11.5^\circ$ (angularly integrated). The convex secondary mirror is aspheric to minimize aberration introduced by the 108° collection angle. The primary is positioned to view the scattering region from 17° above the optical axis at a distance of 100 mm. The emission region is not optically off-axis; it is simply viewed from an off-axis vantage location. The secondary is sized to provide an unobstructed $108^\circ \times 11.5^\circ$ imaging path while simultaneously blocking the direct line-of-sight path from the scattering region down the axis of the system. A Schwarzschild objective is inherently infinity corrected so an achromat tube lens images the scattering region at $10\times$ magnification onto the $500\ \mu\text{m}$ diameter field stop aperture. This field stop defines a $50\ \mu\text{m}$ diameter sampling area of the scattering volume; the third dimension of the volume is defined by the diameter of the probe beam.

The image relay uses a three mirror out-of-plane periscope to rotate the image of the field stop by the 56° angle between the probe beam and the horizontal plane of the recording system. The periscope also points and centers the imaging path into the spectrometer to ensure the central wavelength is parallel to the plane of the system after diffraction. A 20-nm wide, 532-nm central wavelength, optical notch filter in collimated space blocks the ion-acoustic wave feature. A lens located near the field stop introduces very little power into the near-field image at the field stop, but demagnifies the far-field image of the field stop by $10\times$ at the detector surface. The result is a 1:1 spatial image of the scattering region at every angle in the vertical direction at the detector. This convolved with the detector's spatial impulse response determines the 1° angular resolution of the instrument. The final lens in the relay is a cylindrical achromat that creates a line focus from the 11.5° collection angle in the spectrometer's dispersion direction and preserves beam height as a function of emission angle in the 108° collection angle in the spatial direction. This line focus is the effective input slit to the spectrometer.

The spectrometer is a 400 line/mm transmission grating between $\text{Ø}50\ \text{mm} \times 150\ \text{mm}$ focal length achromats. These $f/3$ achromats accept the 11.5° emission collection angle. The 150 mm focal length provides the linear spectral dispersion at the detector surface to record a 450 nm to 650 nm spectral range with 1 nm spectral resolution. The detector surface can be translated in the dispersion direction to examine different spectral ranges or support different groove density gratings.

III. THEORY

A. Thomson-Scattering Theory

Thomson scattering is the elastic scattering of photons off electrons. This results in scattered photons that contain information about the number and velocities of the electrons. In the case of a plasma, the electrons are distributed in velocity space according to the electron velocity distribution function, and therefore the Thomson-scattered spectrum contains this information.

Thomson scattering is broken into two regimes, distinguished by the characteristic scale length being probed ($1/k$). In the non-collective regime ($1/k\lambda_D < 1$), the scale length is smaller than the electron Debye length (λ_D) and the power scattered is directly proportional to the electron velocity distribution function. In the collective regime, the scale length is larger than the electron Debye length ($1/k\lambda_D > 1$) and the scattering off correlated electrons interferes constructively, resulting in peaks in the spectrum that correspond to thermal fluctuations in the plasma. In this regime, the power scattered is dependent on the distribution function and its derivative.

While both regimes can be used to measure the electron distribution function, experimental limitations hamper their utility. The small electron scattering cross section restricts non-collective Thomson scattering to measuring the bulk of the distribution function where the scattering signal exceeds the thermal background. Filamentation and other laser-plasma instabilities, caused by an intense probe beam, further constrain single-shot non-collective measurements to a couple orders of magnitude. Collective Thomson scattering has an improved signal-to-noise, but is less sensitive to the distribution function at frequencies far from the resonance due to the low scattering signal. These restrictions have limited distribution function measurements to the bulk of the distribution function⁴⁰ in the case of non-collective scattering, or to a predetermined class of distributions in the case of collective scattering.^{25,38}

B. Angularly Resolved Thomson Scattering Theory

Angularly resolved Thomson scattering can measure the electron distribution function over many orders of magnitude by simultaneously collecting light scattered from fluctuations

with a large range of wave-vectors. The probed wave-vector is related to the scattering angle by $k^2 = k_0^2 + k_s^2 - 2k_0k_s \cos \theta$, where the scattering angle (θ) is angle between the probe beam ($k_0 = 2\pi/\lambda_0$) and the scattering directions ($k_s = 2\pi/\lambda_s$). λ_0 and λ_s are the probe laser wavelength and scattered wavelength in the plasma, respectively. Therefore, the Thomson-scattering spectrum dispersed in scattering angle measures a range of k -vectors that correspond to a range of $1/k\lambda_D$.

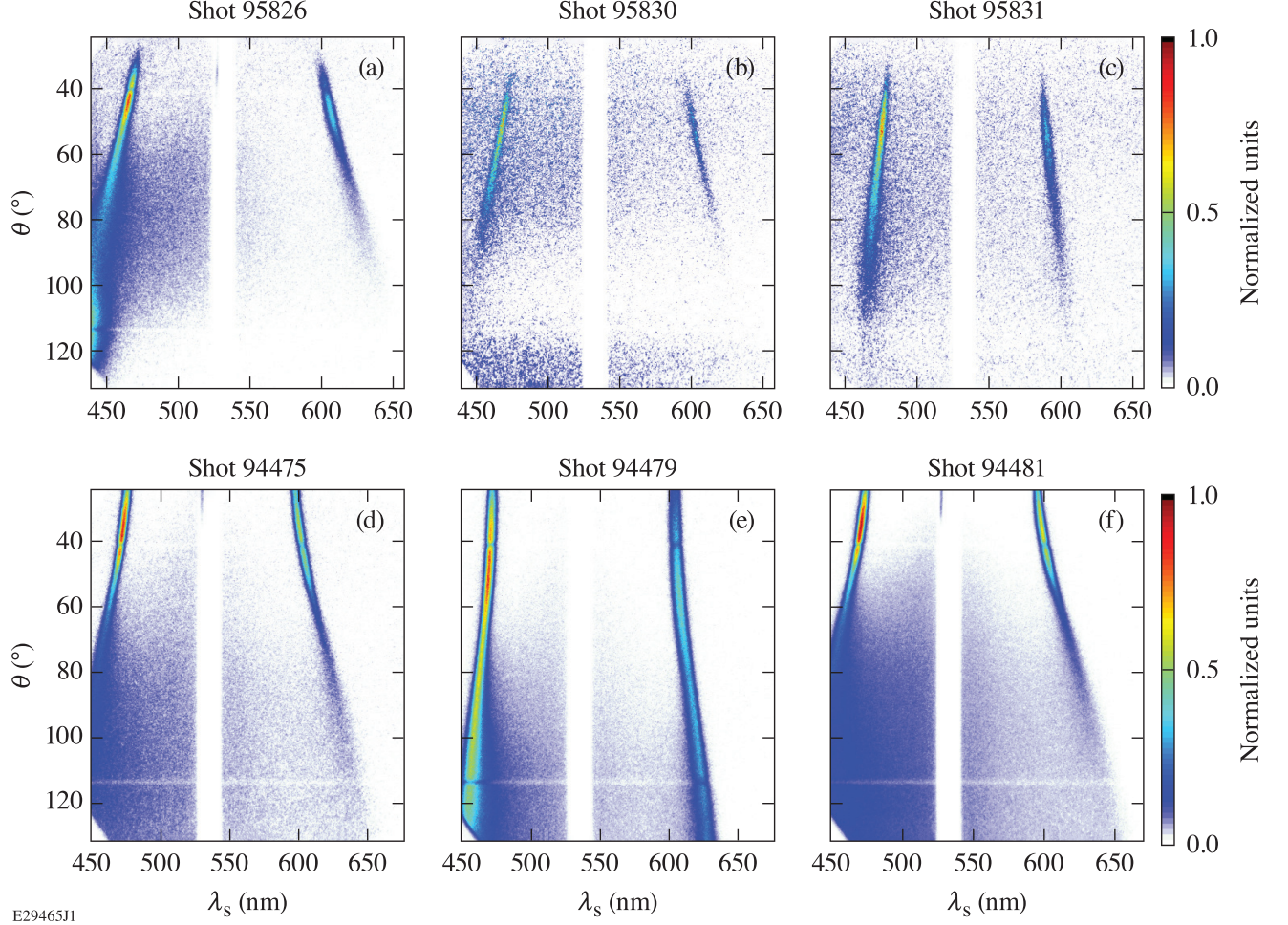
The power of the scattered light as a function of wavelength and angle was related to the electron distribution function,

$$P_s(\lambda_s, \theta) = n_e P_0 r_0^2 c L \left| \hat{s} \times (\hat{s} \times \hat{E}_0) \right|^2 \left(\frac{2\lambda_0}{\lambda_s^3} - \frac{1}{\lambda_s^2} \right) S(x(\lambda_s, \theta)), \quad (1)$$

where the first term contains information about the electron density, probe power (P_0), and the length of the scattering volume (L), r_0 is the classical electron radius. The second term is the scattering efficiency, based on the observation direction (\hat{s}) and probe polarization direction (\hat{E}_0), since Thomson scattering is a dipole scattering process the emission is maximal when observing perpendicular to the polarization. The third term is the first-order relativistic correction,⁴⁵ which accounts for the “relativistic headlight” and $\mathbf{v} \times \mathbf{B}$ effects for electrons up to ~ 5 keV. Finally the collisionless dynamic form factor, which produces the spectral shape, is given by²⁶,

$$S(x) \simeq \left| \frac{1}{1 + \chi_{e,Re}[x] + i\chi_{e,Im}[x]} \right|^2 f_e[x], \quad (2)$$

where f_e is the one-dimensional (1-D) electron distribution function, χ_e is the electron susceptibility, and $x = \omega/kv_{th}$ is the normalized phase velocity. $v_{th} = \sqrt{T_e/m_e}$ is the electron thermal velocity and the frequency of the probed fluctuation is $\omega = 2\pi c \left(\frac{1}{\lambda_s} - \frac{1}{\lambda_0} \right)$. This normalization removes temperature as a parameter and it allows representing all Maxwellian distributions regardless of temperature with a single function. The ion dependence in the dynamic form factor was removed because the measurements were made only for $\omega/k \gtrsim v_{th}$ where the ion contribution is negligible. The one dimensional electron distribution function $f_e[x]$ was projected onto the probed fluctuations. The square brackets are used to denote a discrete domain for the electron distribution function defining it as a set of points instead of a continuous function. The real and imaginary parts of the electron susceptibility are given



E29465J1

FIG. 3. Angularly resolved Thomson-scattering data from six shots. The data was taken in (a,b,c,f) krypton, (d) hydrogen, and (e) argon plasmas. Plasma conditions for each shot are given in Table I.

by⁴⁶,

$$\begin{aligned}
 \chi_{Re} &= -\frac{1}{k^2 \lambda_D^2} \mathcal{P} \int_{-\infty}^{\infty} \frac{\partial f_e / \partial x'}{x' - x} dx', \\
 \chi_{Im} &= -\frac{\pi}{k^2 \lambda_D^2} \left. \frac{\partial f_e}{\partial x'} \right|_x,
 \end{aligned} \tag{3}$$

where $\lambda_D = v_{th} / \omega_{pe}$ and ω_{pe} is the electron plasma frequency.

Shot Number	Gas	I_{UV}^{total} (10^{15} W/cm 2)	Temperature (keV)	Electron Density (10^{20} cm $^{-3}$)
95826	Krypton	2.8	1.34 ± 0.23	0.466 ± 0.058
95830	Krypton	1.2	0.99 ± 0.24	0.408 ± 0.061
95831	Krypton	0.84	0.50 ± 0.11	0.349 ± 0.045
94475	Argon	2.8	1.04 ± 0.13	0.418 ± 0.043
94479	Hydrogen	2.6	0.499 ± 0.078	0.471 ± 0.043
94481	Krypton	2.8	1.16 ± 0.14	0.428 ± 0.042

TABLE I. Gas, heating laser intensity, and plasma conditions for six shots found using an iterative gradient descent algorithm. The uncertainty represents the standard deviations from Monte Carlo analysis on these measurements.

IV. RESULTS

Figure 3 shows angularly resolved Thomson-scattering data from six different experiments. The collective Thomson-scattering peaks from electron plasma waves can be seen as a function of angle. The amplitude of the features decrease and the features become broader as the scattering angle increases. For each data shot, a second shot was taken to record a background spectrum by maintaining the same plasma conditions and turning off the probe beam. The background spectrum has been subtracted from the results presented in Fig. 3.

The gas type, heater beam intensity, measured density, and electron temperature for each shot are shown in Table I. The density was fairly consistent across the shots, with a shot-to-shot rms variation of 13%. Shot 95831 was the only shot with the delayed probe configuration (probing after the heating lasers were turned off), providing more time for the plasma to expand and cool. The variation in electron temperatures was due to differences in laser intensities and heating efficiencies.

The electron velocity distribution function measured in the spectra (Fig. 3) and plasma conditions (Table I) were determined simultaneously using an iterative gradient descent algorithm. A numerical distribution function ($f_e[x]$) was used to forward calculate a fluctuation spectrum (Eq. 2). This spectrum was used to calculate the synthetic power scattered (Eq.

1), which was compared to the experimentally measured spectrum using,

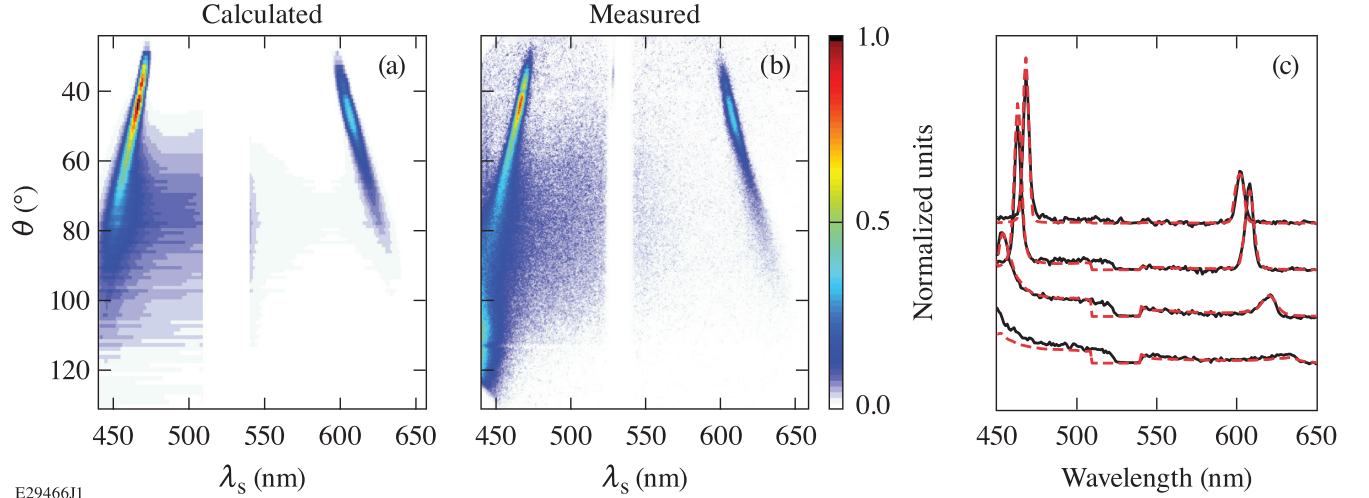
$$\chi^2 = \sum_{\lambda_s} \sum_{\theta=40^\circ}^{115^\circ} \frac{[P_m(\lambda_s, \theta) - P_s(\lambda_s, \theta)]^2}{\sigma^2}. \quad (4)$$

The variation of the data, $\sigma \sim 5\%$, was found by examining the variation in the spectrum at large wavelengths. The region with scattering angles $< 40^\circ$ was excluded because accurate calculation required orders of magnitude higher velocity space resolution. Above a scattering angle of 110° the spectra generally lacked sufficient signal and were dominated by noise.

A minimization of χ^2 over 69 free parameters defining the distribution function (64 points), plasma conditions (n_e and T_e), and scale parameters (3 parameters) was performed on each shot. The most computationally expensive step was computing the susceptibility (Eq. 3). The real part of the susceptibility was solved using the method of rational integration.⁴⁷ Furthermore, to prevent numerical discontinuities in the susceptibility from the discrete distribution function, exponential interpolation was used to produce a continuous distribution function. Convergence was improved by performing a set of sequential fits with increasing number of distribution function points. Fewer points provided significantly better convergence and starting points for the subsequent minimizations closer to the optimal values. It was found that ~ 9 distribution points per thermal velocity (64 points spanning $0 - 7v_{th}$) was optimal for balancing computation time and resolving the distribution function.

Figure 4(a) shows the final spectrum calculated using the measured distribution function for shot 95826. Comparing to the experimental spectrum [Fig. 4(b)], the calculated spectrum qualitatively reproduces the measured spectrum in angle and wavelength across the entire spectral range [Fig. 4(c)]. Small discrepancies occur at small scattering angles due to numerical artifacts and at high scattering angle where there is a small clip in the data. The spectrum at 107° [Fig. 4(c)] shows a small discrepancy between measured and calculated blue peaks, which is a result of Thomson scattering from the UV heater beams that was not completely subtracted with the background.

In order to match the measured spectrum, the effects of temporal gradients, finite angles, and instrument response were included in the calculation. The instrument response function was included by convolving the scattered power with a 2-D Gaussian with a spectral width of 1 nm and angular width of 1° , matching the measured instrument response function. The curvature of the primary mirror and finite solid angle of the probe beam result in a small



E29466J1

FIG. 4. (a) Calculated and (b) measured spectra from a krypton plasma used to determine the measured electron distribution shown in Fig. 5. (c) The measured (black curve) and calculated (red curve) spectra at four scattering angles (51° , 70° , 88° , and 107°) have been arbitrarily spaced along the y-axis.

change in the scattering angle as a function of height on the mirror. This was included in calculation by treating each angle at the CCD as a weighted sum of the true constituent scattering angles.

A temporally resolved Thomson-scattering diagnostic⁴⁸ was used on each shot to diagnose the temporal gradients in plasma conditions. Combining the data from the two types of Thomson scattering, a self consistent set of plasma conditions and distribution function was found⁴². The temporal gradient was included in the numerical distribution function analysis by integrating over spectra with the same distribution function but a range of plasma conditions.

A. Inverse Bremsstrahlung Heating

The distribution function measurements were made in a plasma where inverse bremsstrahlung heating was predicted to drive non-Maxwellian distribution functions. Inverse bremsstrahlung occurs when an electron oscillating in the electric field of the laser collides with an ion, allowing the electron to retain some of the momentum it gained from the laser field, thereby transferring energy from the field to the electron. The larger electron-ion collision rate for

slow electrons suggests that this mechanism preferentially heats slow electrons leading to a flattening of the electron distribution.⁷ Fokker-Planck simulations showed that the degree to which the distribution is flattened depends on the relative strength of inverse bremsstrahlung heating and thermalization due to electron-electron collisions, which was parameterized as $\alpha = Zv_{osc}^2/v_{th}^2$ (Ref. 8), where v_{osc} is the velocity of electrons oscillating in the laser field. The resultant distribution has a super-Gaussian shape,

$$f_m(v) = C_m \exp \left[- \left(\frac{v}{a_m v_{th}} \right)^m \right], \quad (5)$$

with super-Gaussian order

$$m(\alpha) = 2 + \frac{3}{1 + 1.66/\alpha^{0.724}}, \quad (6)$$

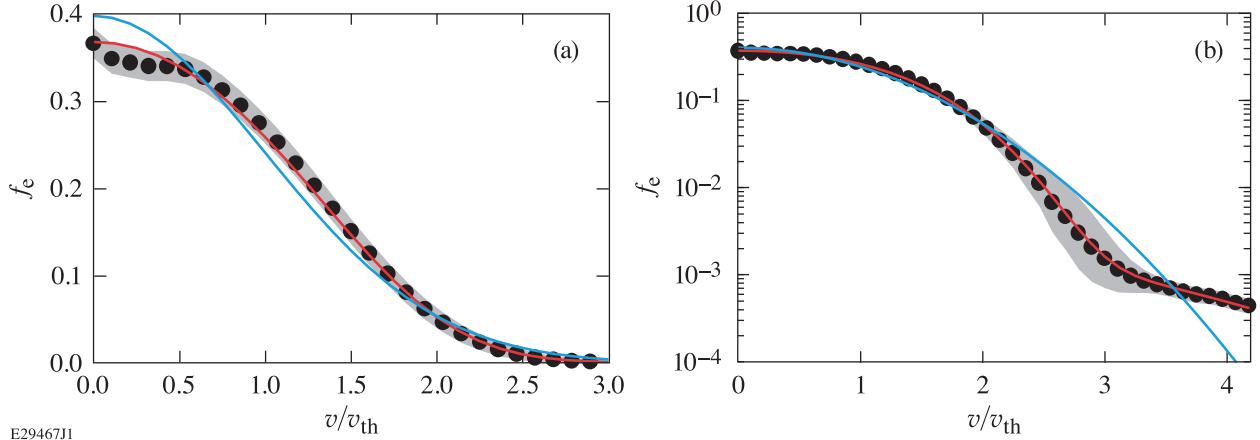
where the normalization constants (C_m , a_m) maintain the standard definitions of the first three moments (e.g. $\frac{3}{2}n_e T_e = \int \frac{1}{2}m_e v^2 f_m(v) d^3\mathbf{v}$).

Multiple theoretical and simulation studies have shown this modification to the bulk ($v/v_{th} < 3$) of the distribution function, but the shape of the tail ($v/v_{th} > 3$) has been debated.^{13–15,19} One model of particular relevance to this experimental configuration showed that since the electron oscillations are anisotropic, aligned with the laser polarization, the collision operator is modified.¹⁵ This leads to an altered tail in the isotropic distribution function. This revised electron distribution function is super-Gaussian in the bulk and transitions to Maxwellian in the tail.

B. Distribution functions

Figure 5 shows the measured numerical distribution function from a krypton plasma. This numerical distribution function was determined without making any assumptions about the shape or underlying physics. It shows a more flat-topped profile than the Maxwellian distribution [Fig. 5 (a)] and an elevated tail [Fig. 5 (b)]. These features are consistent with expectations based on inverse bremsstrahlung heating. Agreement with inverse bremsstrahlung theory motivated a description using a reduced model comprised of super-Gaussian and Maxwellian functions,

$$f_e(x) = A_1 \exp \left[- \left(\frac{x}{x_1} \right)^m \right] + \exp[A_2] \exp \left[- \left(\frac{x}{x_2} \right)^2 \right]. \quad (7)$$



E2946711

FIG. 5. Measured electron distribution functions (black points) on a (a) linear and (b) logarithmic scale. A super-Gaussian plus Maxwellian model (red curve) was compared to the data. A 90% confidence interval (gray) was computed from the super-Gaussian plus Maxwellian model. A Maxwellian distribution function (blue curve) is shown for reference.

This model reproduced the distribution function both in the bulk and tail (Fig. 5), but tends to perform worse near the peak ($v < 0.5v_{th}$). Because this model is less precise, owing to the fewer degrees of freedom, it is unable to capture all the detail of the measured distribution function. Consequently, spectra calculated from this reduced model provide a slightly worse match to the measured spectra. While less accurate, this physically motivated reduced model has the advantage of being more computationally tractable.

V. CONFIDENCE ANALYSIS

A 90% confidence interval was determined for the measured electron distribution function using the reduced model (Eq. 7). This confidence interval is shown as a gray region in Figure 5. Many of the same difficulties faced in calculating the numerical electron distribution function complicated the uncertainty analysis, preventing direct calculation of the uncertainties on the numerical distribution function. The high dimensionality led to saddle points that prevented the use of Hessian based uncertainty calculations, while more complicated methods such as a Monte Carlo or grid analysis were too computationally expensive. The excellent agreement of the reduced model provided an alternative by defining the plasma conditions and distribution function in 7 parameters, (electron temperature, electron density, and the 5

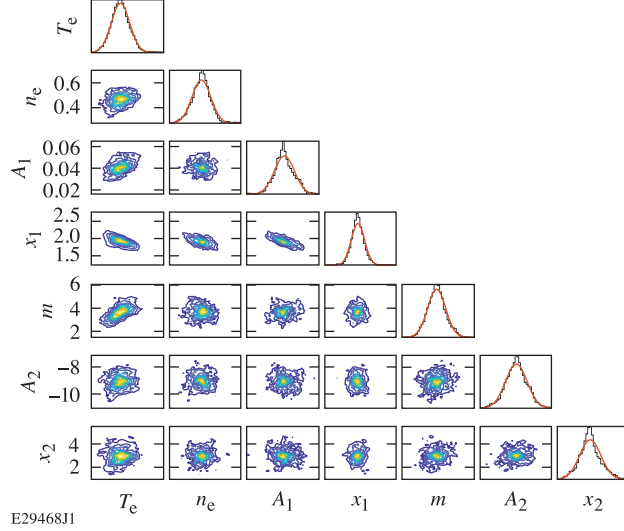


FIG. 6. Marginal probability distributions of each parameter in the reduced model (Eq. 7) determined from Monte Carlo analysis.

parameters of the reduced model). In this lower dimensional space, it was computationally tractable to perform uncertainty analysis using Markov-chain Monte Carlo. Two additional parameters were added to determine the sensitivity to calibration of the wavelength axis. The calibration uncertainty was included to achieve a confidence region on the distribution function, which accounts for statistical (model) and instrumental sources of error.

Figure 6 shows the 2-parameter joint and single parameter marginal distributions from the Monte Carlo analysis. Numerous covariances can be seen between parameters as the contours are rotated ellipsoids. For two uncorrelated parameters, the contours of equal probability are circles, while two perfectly correlated parameters would result in elliptical contours with the semi-major axis aligned to $y = x$. The width parameter of the super-Gaussian (x_1) is inversely correlated with temperature, density, and amplitude. These are all related to maintaining the normalization of the distribution function. The positive correlation of the super-Gaussian order (m) and temperature is related to maintaining the width of the peaks in the Thomson-scattering spectrum.

The uncertainty analysis was preformed using the Metropolis-Hastings algorithm with 72 walkers and 3,000 steps per walker. A burn-in period of 50 steps was found to sufficiently remove bias from the initial conditions of the walkers. A uniform prior was used on the parameters, but a lower reflective boundary at a temperature of 1 eV and a density of 10^{16} cm^{-3} prevented nonphysical steps from causing algorithm-based errors.

Shot Number	A_1	x_1	m	A_2	x_2
95826	0.0413 ± 0.0068	1.91 ± 0.14	3.67 ± 0.57	-9.07 ± 0.60	3.02 ± 0.67
95830	0.0346 ± 0.0070	1.94 ± 0.20	3.57 ± 0.63	-6.54 ± 0.55	2.04 ± 0.55
95831	0.0510 ± 0.0055	1.58 ± 0.11	2.36 ± 0.35	-8.14 ± 0.42	2.70 ± 0.36
94475	0.0245 ± 0.0045	2.17 ± 0.17	4.22 ± 0.35	-6.74 ± 0.41	1.75 ± 0.22
94479	0.0360 ± 0.0044	1.82 ± 0.11	2.60 ± 0.37	-6.36 ± 0.43	1.60 ± 0.47
94481	0.0309 ± 0.0051	2.031 ± 0.051	3.92 ± 0.24	-9.15 ± 0.31	1.97 ± 0.31

TABLE II. Reduced-model parameters from Monte Carlo analysis for six shots. The uncertainty represents the standard deviation on these values.

Each of the single-parameter marginal distributions was fit with a Gaussian (Fig. 6) to determine the mean and variance. The standard deviation of the plasma conditions was given as an uncertainty on the conditions measured with the numerical distribution function analysis in Table I. The mean and standard deviation for each of the reduced-model parameters is shown in Table II. These uncertainties are dependent on two factors, how much the spectrum changes in response to the parameter and how much variation can be seen in the data. Using electron temperature (T_e) as an example, changes can broaden the peak in wavelength. However, the spectral instrumental response sets a minimum on the measured broadening. Noise in the data allows a range of values to be contained within the bounds of the data, making it difficult to distinguish whether a mismatch between a given data point and theoretical point is due to fluctuation or an incorrect parameter.

The 90% confidence interval on the distribution function (Fig. 5) was determined with standard error propagation techniques of the uncertainties in Table II. The uncertainty on the distribution function was,

$$\sigma_{f_e} = \left[\left(\frac{\partial f_e}{\partial A_1} \right)^2 \sigma_{A_1}^2 + \left(\frac{\partial f_e}{\partial x_1} \right)^2 \sigma_{x_1}^2 + \left(\frac{\partial f_e}{\partial m} \right)^2 \sigma_m^2 + \left(\frac{\partial f_e}{\partial A_2} \right)^2 \sigma_{A_2}^2 + \left(\frac{\partial f_e}{\partial x_2} \right)^2 \sigma_{x_2}^2 \right]^{1/2}. \quad (8)$$

A multiplier on standard deviation for each shot was determined by integrating over the 9-dimensional probability distribution until 90% probability was achieved. Strictly, this is a confidence interval on the reduced model, but is reported on the numerical distribution.

Figure 7 shows the scaling of the super-Gaussian order (m) with the Langdon parameter (α) and super-Gaussian width (x_1). When using the super-Gaussian plus Maxwellian model, good agreement is found with the expected scaling for m (Eq. 6). A notable outlier is shot

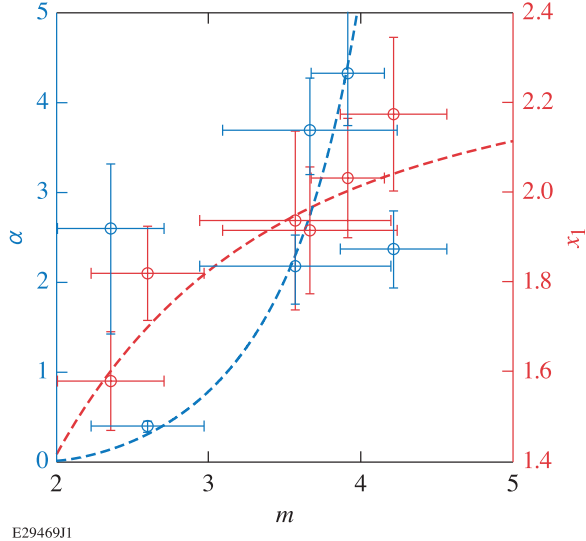


FIG. 7. Scaling of the super-Gaussian order with relative strength of inverse bremsstrahlung heating to electron-electron collisions (α) and super-Gaussian width (x_1). The values for each of the six shots are plotted with error-bars showing one standard deviation. The dashed lines are the expected scaling relations from Fokker-Planck simulations.

95831, which was measured after the heating beams were turned off, giving the plasma time to cool and the distribution time to Maxwellianize. The scaling of x_1 with m was found to agree with the data, as was expected to maintain the definition of temperature as the average kinetic energy.

VI. SUMMARY

Angularly resolved Thomson scattering provides precise measurements of the distribution function over many orders of magnitude. The distribution function was measured without *a priori* knowledge of its shape, and the technique will allow a range of applications to be studied beyond inverse bremsstrahlung heating. The measured distribution functions were determined to be significantly different than a Maxwellian. These differences exist in the bulk, where the distribution function is super-Gaussian, and in the tail, where the distribution function is Maxwellian, but with a different amplitude and width. While these changes can affect many aspects of the plasma's behaviour (laser-plasma interaction, heat flux, and x-ray emission), a reduced model was found that captures these changes. This simplified model, including the contributions of inverse bremsstrahlung and heating isotropy,

can be utilized by hydrodynamic simulations to improve agreement or serve as a basis for further theoretical investigation on the formation of tails.

The uncertainties in the measured distribution functions were due to the experimental limitations in the range of probed wave-vectors and instrumental response. Even with these uncertainties, the electron distribution function was measured to a level of precision more than sufficient to distinguish the distribution from Maxwellian or other functional forms. Understanding the uncertainties in this distribution function analysis is important in determining problems where angularly resolved Thomson scattering can be applied. This is a tool with significant potential to elucidate the detailed physics occurring in plasmas, but an understanding of the uncertainties is required to know if the measured distribution function is distinguishable from other potential solutions.

VII. DATA AVAILABILITY

The data that supports the findings of this study are available within the article, further data is available from the corresponding author upon request.

VIII. ACKNOWLEDGEMENT

LLNL-JRNL-826649

This material is based upon work supported by the Department of Energy National Nuclear Security Administration under Award Number DE-NA0003856, the University of Rochester, and the New York State Energy Research and Development Authority.

This report was prepared as an account of work sponsored by an agency of the U.S. Government. Neither the U.S. Government nor any agency thereof, nor any of their employees, makes any warranty, express or implied, or assumes any legal liability or responsibility for the accuracy, completeness, or usefulness of any information, apparatus, product, or process disclosed, or represents that its use would not infringe privately owned rights. Reference herein to any specific commercial product, process, or service by trade name, trademark, manufacturer, or otherwise does not necessarily constitute or imply its endorsement, recommendation, or favoring by the U.S. Government or any agency thereof. The views and opinions of authors expressed herein do not necessarily state or reflect those of the U.S. Government or any agency thereof.

REFERENCES

- ¹T. E. Tierney IV, D. S. Montgomery, J. F. Benage, F. J. Wysocki, and M. S. Murillo, *J. Phys. A, Math. Gen.* **36**, 5981 (2003).
- ²A. S. Davies, D. Haberberger, J. Katz, S. Bucht, J. P. Palastro, W. Rozmus, and D. H. Froula, *Phys. Rev. Lett.* **122**, 155001 (2019).
- ³G. F. Swadling, C. Bruulsema, F. Fiuza, D. P. Higginson, C. M. Huntington, H. S. Park, B. B. Pollock, W. Rozmus, H. G. Rinderknecht, J. Katz, A. Birkel, and J. S. Ross, *Phys. Rev. Lett.* **124**, 215001 (2020).
- ⁴O. L. Landen and R. J. Winfield, *Phys. Rev. Lett.* **54**, 1660 (1985).
- ⁵J. R. Albritton, E. A. Williams, I. B. Bernstein, and K. P. Swartz, *Phys. Rev. Lett.* **57**, 1887 (1986).
- ⁶P. Helander, H. Smith, T. Fülöp, and L. G. Eriksson, *Phys. Plasmas* **11**, 5704 (2004).
- ⁷A. B. Langdon, *Phys. Rev. Lett.* **44**, 575 (1980).
- ⁸I. V. Igumenshchev, V. N. Goncharov, W. Seka, D. Edgell, and T. R. Boehly, “The effect of resonance absorption in OMEGA direct-drive designs and experiments,” *Phys. Plasmas* **14**, 092701 (2007).
- ⁹M. D. Rosen, H. A. Scott, D. E. Hinkel, E. A. Williams, D. A. Callahan, R. P. Town, L. Divol, P. A. Michel, W. L. Kruer, L. J. Suter, R. A. London, J. A. Harte, and G. B. Zimmerman, “The role of a detailed configuration accounting (DCA) atomic physics package in explaining the energy balance in ignition-scale hohlraums,” *High Energy Density Phys.* **7**, 180–190 (2011).
- ¹⁰W. Davies and S. Ramsden, “Scattering of light from the electrons in a plasma,” *Phys. Lett.* **8**, 179–180 (1964).
- ¹¹J. M. Liu, J. S. De Groot, J. P. Matte, T. W. Johnston, and R. P. Drake, “Measurements of inverse bremsstrahlung absorption and non-maxwellian electron velocity distributions,” *Phys. Rev. Lett.* **72**, 2717–2720 (1994).
- ¹²S. H. Glenzer, W. Rozmus, B. J. MacGowan, K. G. Estabrook, J. D. de Groot, G. B. Zimmerman, H. A. Baldis, J. A. Harte, R. W. Lee, E. A. Williams, and B. G. Wilson, *Phys. Rev. Lett.* **82**, 97 (1999).
- ¹³J. P. Matte, M. Lamoureux, C. Moller, R. Y. Yin, J. Delettrez, J. Virmont, and T. W. Johnston, *Plasma Phys. Control. Fusion* **30**, 1665 (1988).

- ¹⁴S. Brunner and E. Valeo, Phys. Plasmas **9**, 923 (2002).
- ¹⁵E. Fourkal, V. Y. Bychenkov, W. Rozmus, R. Sydora, C. Kirkby, C. E. Capjack, S. H. Glenzer, and H. A. Baldis, Phys. Plasmas **8**, 550 (2001).
- ¹⁶P. Mora and H. Yahi, “Thermal heat-flux reduction in laser-produced plasmas,” Phys. Rev. A **26**, 2259–2261 (1982).
- ¹⁷C. T. Dum, “Anomalous heating by ion sound turbulence,” Phys. Fluids **21**, 945–955 (1978).
- ¹⁸J. Zheng, C. X. Yu, and Z. J. Zheng, “Effects of non-Maxwellian (super-Gaussian) electron velocity distribution on the spectrum of Thomson scattering,” Phys. Plasmas **4**, 2736–2740 (1997).
- ¹⁹M. Krook and T. T. Wu, Phys. Rev. Lett. **36**, 1107 (1976).
- ²⁰R. J. Henchen, M. Sherlock, W. Rozmus, J. Katz, D. Cao, J. P. Palastro, and D. H. Froula, Phys. Rev. Lett. **121**, 125001 (2018).
- ²¹W. Rozmus, T. Chapman, A. Brantov, B. J. Winjum, R. L. Berger, S. Brunner, V. Y. Bychenkov, A. Tableman, M. Tzoufras, and S. Glenzer, “Resonance between heat-carrying electrons and Langmuir waves in inertial confinement fusion plasmas,” Phys. Plasmas **23**, 012707 (2016).
- ²²L. Yin, B. J. Albright, K. J. Bowers, W. Daughton, and H. A. Rose, “Saturation of backward stimulated scattering of a laser beam in the kinetic regime,” Phys. Rev. Lett. **99**, 1–4 (2007).
- ²³H. P. Le, M. Sherlock, and H. A. Scott, “Influence of atomic kinetics on inverse bremsstrahlung heating and nonlocal thermal transport,” Phys. Rev. E **100**, 013202 (2019).
- ²⁴See National Technical Information Service Document DE200114770 (B. B. Afeyan, A. E. Chou, and W. L. Kruer, Lawrence Livermore National Laboratory, ICF Annual Report 1997, Report UCRL-LR-105821-97-2, 1998).
- ²⁵D. Turnbull, A. Colaïtis, A. M. Hansen, A. L. Milder, J. P. Palastro, J. Katz, C. Dorrer, B. E. Kruschwitz, D. J. Strozzi, and D. H. Froula, Nat. Phys. **16**, 181 (2020).
- ²⁶D. H. Froula, S. H. Glenzer, N. C. Luhmann, Jr., and J. Sheffield, *Plasma Scattering of Electromagnetic Radiation: Theory and Measurement Techniques*, 2nd ed. (Academic Press, Amsterdam, 2011).
- ²⁷D. Turnbull, C. Goyon, G. E. Kemp, B. B. Pollock, D. Mariscal, L. Divol, J. S. Ross, S. Patankar, J. D. Moody, and P. Michel, Phys. Rev. Lett. **118**, 015001 (2017).

- ²⁸C. Rousseaux, L. Gremillet, M. Casanova, P. Loiseau, M. Rabec Le Gloahec, S. D. Baton, F. Amiranoff, J. C. Adam, and A. Héron, *Phys. Rev. Lett.* **97**, 015001 (2006).
- ²⁹D. S. Montgomery, R. P. Johnson, J. A. Cobble, J. C. Fernández, E. L. Lindman, H. A. Rose, and K. G. Estabrook, *Laser Part. Beams* **17**, 349 (1999).
- ³⁰S. Depierreux, C. Labaune, J. Fuchs, D. Pesme, V. T. Tikhonchuk, and H. A. Baldis, *Phys. Rev. Lett.* **89**, 045001 (2002).
- ³¹J. L. Kline, D. S. Montgomery, B. Bezzerides, J. A. Cobble, D. F. Dubois, R. P. Johnson, H. A. Rose, L. Yin, and H. X. Vu, *Phys. Rev. Lett.* **94**, 175003 (2005).
- ³²D. R. Gray and J. D. Kilkenny, *Plasma Phys.* **22**, 81 (1980).
- ³³S. H. Glenzer, W. E. Alley, K. G. Estabrook, J. S. De Groot, M. G. Haines, J. H. Hammer, J. P. Jadaud, B. J. MacGowan, J. D. Moody, W. Rozmus, L. J. Suter, T. L. Weiland, and E. A. Williams, *Phys. Plasmas* **6**, 2117 (1999).
- ³⁴T. Hori, M. D. Bowden, K. Uchino, and K. Muraoka, “Measurement of non-Maxwellian electron energy distributions in an inductively coupled plasma,” *Appl. Phys. Lett.* **69**, 3683–3685 (1996).
- ³⁵K. V. Beausang, S. L. Prunty, R. Scannell, M. N. Beurskens, M. J. Walsh, and E. De La Luna, “Detecting non-Maxwellian electron velocity distributions at JET by high resolution Thomson scattering,” *Rev. Sci. Instrum.* **82**, 033514 (2011).
- ³⁶S. V. Lebedev, L. Suttle, G. F. Swadling, M. Bennett, S. N. Bland, G. C. Burdiak, D. Burgess, J. P. Chittenden, A. Ciardi, A. Clemens, P. De Grouchy, G. N. Hall, J. D. Hare, N. Kalmoni, N. Niase, S. Patankar, L. Sheng, R. A. Smith, F. Suzuki-Vidal, J. Yuan, A. Frank, E. G. Blackman, and R. P. Drake, “The formation of reverse shocks in magnetized high energy density supersonic plasma flows,” *Phys. Plasmas* **21**, 056305 (2014).
- ³⁷S. Frydrych, J. Vorberger, N. J. Hartley, A. K. Schuster, K. Ramakrishna, A. M. Saunders, T. van Driel, R. W. Falcone, L. B. Fletcher, E. Galtier, E. J. Gamboa, S. H. Glenzer, E. Granados, M. J. MacDonald, A. J. MacKinnon, E. E. McBride, I. Nam, P. Neumayer, A. Pak, K. Voigt, M. Roth, P. Sun, D. O. Gericke, T. Döppner, and D. Kraus, “Demonstration of X-ray Thomson scattering as diagnostics for miscibility in warm dense matter,” *Nat. Commun.* **11**, 2620 (2020).
- ³⁸A. L. Milder, H. P. Le, M. Sherlock, P. Franke, J. Katz, S. T. Ivancic, J. L. Shaw, J. P. Palastro, A. M. Hansen, I. A. Begishev, W. Rozmus, and D. H. Froula, *Phys. Rev. Lett.* **124**, 025001 (2020).

- ³⁹C. Zhang, C. K. Huang, K. A. Marsh, C. E. Clayton, W. B. Mori, and C. Joshi, “Ultrafast optical field-ionized gases-A laboratory platform for studying kinetic plasma instabilities,” *Sci. Adv.* **5**, eaax4545 (2019).
- ⁴⁰N. J. Peacock, D. C. Robinson, M. J. Forrest, P. D. Wilcock, and V. V. Sannikov, *Nature* **224**, 488 (1969).
- ⁴¹S. Segre and L. Pieroni, “Measurement of non-maxwellian electron distribution functions in hot plasma and the importance for Thomson scattering diagnostics,” *Phys. Lett. A* **51**, 25–26 (1975).
- ⁴²A. L. Milder, J. Katz, R. Boni, J. P. Palastro, M. Sherlock, W. Rozmus, and D. H. Froula, “Measurements of non-Maxwellian electron distribution functions and their effect on laser heating,” accepted to *Physical Review Letters*.
- ⁴³T. R. Boehly, R. S. Craxton, T. H. Hinterman, J. H. Kelly, T. J. Kessler, S. A. Kumpan, S. A. Letzring, R. L. McCrory, S. F. B. Morse, W. Seka, S. Skupsky, J. M. Soures, and C. P. Verdon, *Rev. Sci. Instrum.* **66**, 508 (1995).
- ⁴⁴A. M. Hansen, D. Haberberger, J. Katz, D. Mastrosimone, R. K. Follett, and D. H. Froula, *Rev. Sci. Instrum.* **89**, 10C103 (2018).
- ⁴⁵J. S. Ross, S. H. Glenzer, J. P. Palastro, B. B. Pollock, D. Price, L. Divol, G. R. Tynan, and D. H. Froula, *Phys. Rev. Lett.* **104**, 105001 (2010).
- ⁴⁶J. P. Palastro, J. S. Ross, B. Pollock, L. Divol, D. H. Froula, and S. H. Glenzer, *Phys. Rev. E* **81**, 036411 (2010).
- ⁴⁷T. Chapmann, Lawrence Livermore National Laboratory (private communication, 2019).
- ⁴⁸J. Katz, R. Boni, C. Sorce, R. Follett, M. J. Shoup III, and D. H. Froula, *Rev. Sci. Instrum.* **83**, 10E349 (2012).

This work was performed under the auspices of the U.S. Department of Energy by Lawrence Livermore National Laboratory under Contract No. DE-AC52-07NA27344. This document was prepared as an account of work sponsored by an agency of the United States government. Neither the United States government nor Lawrence Livermore National Security, LLC, nor any of their employees makes any warranty, expressed or implied, or assumes any legal liability or responsibility for the accuracy, completeness, or usefulness of any information, apparatus, product, or process disclosed, or represents that its use would not infringe privately owned rights. Reference herein to any specific commercial product, process, or service by trade name, trademark, manufacturer, or otherwise does not necessarily constitute or imply its endorsement, recommendation, or favoring by the United States government or Lawrence Livermore National Security, LLC. The views and opinions of authors expressed herein do not necessarily state or reflect those of the United States government or Lawrence Livermore National Security, LLC, and shall not be used for advertising or product endorsement purposes. The data that support the findings of this study are available from the corresponding author upon reasonable request.